Heterostructure with tightly-bound interface between In_2O_3 hollow fiber and $ZnIn_2S_4$ nanosheet toward efficient visible light driven hydrogen evolution

Ping Lu [a,b], Ke Liu [b], Yan Liu [b], Zhilin Ji [b], Xiaoxia Wang [b], Bin Hui [b], Yukun Zhu [b,*], Dongjiang Yang [b,*], Luhua Jiang [a,*]

[a] College of Materials Science and Engineering, Qingdao University of Science and Technology, Qingdao 266042, PR China
[b] School of Environmental Science and Engineering, State Key Laboratory of Bio-fibers and Eco-textiles, Qingdao University, Qingdao 266071, PR China

ARTICLE INFO

ABSTRACT

Visible-light-driven photocatalytic hydrogen evolution is considered as one of the most useful approaches to produce renewable fuels from abundant resources. Indium oxide (In_2O_3) has attracted much attention in the field of solar hydrogen production due to its moderate band gap, which can be driven by visible light easily. However, the efficiency of hydrogen evolution reaction (HER) of In_2O_3 is currently unsatisfactory. To enhance the HER efficiency of In_2O_3, herein, sandwich-structured $In_2O_3/ZnIn_2S_4$ heterostructure was precisely constructed via in-situ growth of $ZnIn_2S_4$ nanosheets on the In_2O_3 hollow fibers. The fabricated $In_2O_3/ZnIn_2S_4$ heterostructure exhibited a significantly enhanced photocatalytic HER activity of 2.18 mmol/g/h as compared to pure In_2O_3 and $ZnIn_2S_4$. Such efficient photocatalytic hydrogen production is attributed to the tightly-bound interface between (001) planes of flake $ZnIn_2S_4$ and (222) planes of In_2O_3. Experimental and theoretical investigation indicates compactly interface enabling efficient charge transfer and separation, which benefited the excellent photocatalytic HER performance.

1. Introduction

To address the challenges of energy shortage and environmental pollution, the potential of photocatalytic water splitting technology under visible light has been widely explored [1–5]. The development of efficient and stable photocatalysts is essential for this field. TiO_2 was first used in photocatalytic due to its low price, the earth abundance, high chemical stability, safety and strong oxidizing potential. However, its photoactivity is mostly limited to the UV region because of its wide bandgap (3.0–3.2 eV). Thus, researchers have tried to explore photocatalysts driven by visible light, which accounts for 45% of incident solar energy. R. Asahi first doped nitrogen into substitutional sites of TiO_2 to produce visible-light photocatalysts [6]. After that, many visible light driven photocatalysts have been explored, such as $g-C_3N_4$ [5], and metal sulfides represented by CdS [7–9]. Recently, indium oxide (In_2O_3), a semiconductor with a moderate band gap energy of approximately 2.8 eV, has attracted considerable attention in photocatalysis, since it possesses favorable conductivity, excellent chemical stability, and unique optical and electrical characteristics [10–12]. Particularly,

its conduction band (CB) edge is at approximately − 0.6 eV, which is very suitable for hydrogen production. However, the efficiency of hydrogen evolution reaction (HER) of In_2O_3 is currently unsatisfactory, primarily due to the high recombination rate of photogenerated charge carriers. Especially for cubic In_2O_3, is easier to form oxygen vacancies, which accelerate the recombination of electrons and holes [13,14].

Some strategies, such as morphology control [15], loading co-catalysts [16,17], and constructing heterostructures [18,19], have been utilized to enhance the photocatalytic HER performance. Among them, constructing heterostructures can achieve appropriate band alignment between the different components, which is crucial for efficient transfer of photo-generated charge carriers, making interface contact mediation a critical aspect [20–22]. In a type-II heterostructure, all of the semiconductor photocatalysts can be excited by the light radiation to induce the electron-hole pairs, and the electrons generated in the CB of photocatalyst I (PC I) will transfer to the CB of photocatalyst II (PC II) due to the potential difference. At the same time, the photo-induced holes in these two semiconductors may move in opposite routes. Thus, the photo-induced electrons could aggregate in the CB of

PC II to induce the reduction reaction and the holes could converge in the valance band (VB) of PC I to induce the oxidation reaction, respectively. The special transfer process improves the separation of photo-induced charges in the region space and reduces the opportunity of their recombination, thus significantly improving the energy conversion efficiency of photocatalysts. Much recently, several In_2O_3-based heterostructures (C_3N_4/In_2O_3 [23], CdS/In_2O_3 [24], etc.) have been synthesized with certain improvements in charge transfer. However, the lattice matching degree of these heterostructures usually affected due to different crystal structures and lattice parameters, limiting their ability to facilitate spatial charge separation. The mismatched lattice of heterostructured catalysts greatly increases the impedance of charge immigration at the interfaces, leading to the accumulation and recombination of photogenerated electrons and holes [25,26]. $ZnIn_2S_4$ has been widely employed in photocatalysts due to its narrow bandgap and favorable physical/chemical properties [27–30]. Moreover, $ZnIn_2S_4$ shows similar lattice parameters with In_2O_3, when the (222) of In_2O_3 and the (001) of $ZnIn_2S_4$ are combined, the lattice mismatch is less than 5%, indicating $ZnIn_2S_4$ could match well with In_2O_3. Thus, $ZnIn_2S_4$ is a promising candidate for coupling with In_2O_3 to form $In_2O_3/ZnIn_2S_4$ heterostructure with high visible light photocatalytic activities. At present, the studies on $In_2O_3/ZnIn_2S_4$ heterostructure mainly focus on the HER performance improvement. However, the investigation of the $In_2O_3/ZnIn_2S_4$ phase interface has rarely reported [31,32].

In this study, $In_2O_3/ZnIn_2S_4$ heterostructure were successfully constructed using In_2O_3 hollow fibers as precursors derived from alginate fibers. Subsequently, a flake-like $ZnIn_2S_4$ layers were loaded onto the surface of the In_2O_3 hollow fibers using a chemical bath approach. The obtained $In_2O_3/ZnIn_2S_4$ heterostructure photocatalyst shows much higher HER performance than that of pure In_2O_3 hollow fibers and $ZnIn_2S_4$, achieving a HER rate of up to 2.18 mmol/g/h. It was seen that similar lattice parameters of In_2O_3 and $ZnIn_2S_4$ caused higher lattice matching degree of their heterostructure, thus compact interface between the (222) plane of In_2O_3 and the (001) plane of $ZnIn_2S_4$ was fabricated. Density functional theory (DFT) calculation results prove that compactly interface accelerates charge transfer and separation, which effectively enhances the photocatalytic HER performance. In this study, we aim to investigate the interfacial growth mode between In_2O_3 and $ZnIn_2S_4$ and the relationship with HER performance. This provides a theoretical basis and new ideas for the construction of heterostructures.

2. Experimental section

2.1. Synthesis of $In_2O_3/ZnIn_2S_4$ heterostructure composites

2.1.1. Synthesis of In_2O_3 hollow fibers

10 g of calcium alginate fibers were added to a solution of 0.1 M HCl and stirred for 30 min. The mixture was then added to a solution of $(CH_3COO)_3In$ and stirred for 2 h to obtain the In-alginate fiber. The resulting material was calcined in a muffle furnace to obtain In_2O_3 hollow nanotubes.

2.1.2. Synthesis of $In_2O_3/ZnIn_2S_4$ heterostructure

$In_2O_3/ZnIn_2S_4$ were synthesized as previous work [32–34]. 50 mg of In_2O_3 was added to 20 mL of H_2O and stirred for 30 min. Then, different amount of $InCl_2$ (1 mM, 2 mM, 3 mM), $ZnCl_2$ (1 mM, 2 mM, 3 mM), and thioacetamide (TAA) (2 mM, 4 mM, 6 mM) were added to the solution and stirred for another 30 min to obtain a series of samples with different amount of $ZnIn_2S_4$. The resulting mixture was heated to 80 °C and stirred for 2 h. After cooled to room temperature, the as-prepared products were rinsed with deionized water and ethanol. The content of In_2O_3 was 11.0, 5.6, and 3.8 wt% for 1, 2, and 3 mM $In_2O_3/ZnIn_2S_4$, respectively. The preparation of $ZnIn_2S_4$ was similar to that of $In_2O_3/ZnIn_2S_4$ without adding of In_2O_3.

2.2. Characterization

X-ray diffraction (XRD) was performed on DX2700 operating at 40 kV and 30 mA equipped with Cu Kα radiation (λ = 1.5418 Å). The morphology of the samples was conducted by an FEI Magellan 400 scanning electron microscope (SEM) and a JEOL JEM-2100 F transmission electron microscope (TEM). X-ray photoelectron spectroscopy (XPS) was carried out on ESCALAB 250XL electron spectrometer (Thermo Scientific Corporation). The diffuse reflectance spectra were conducted with Agilent Cary 5000 UV-Vis-NIR spectrophotometer using an integrated sphere accessory. Electron paramagnetic resonance experiments were carried out on a Bruker A300 X-band spectrometer. Photoluminescence spectra were carried out using Edinburgh FLS980 fluorescence spectrometer with an excitation wavelength of 340 nm.

2.3. Photocatalytic performance measurements

The photocatalytic hydrogen production experiments were carried out at room temperature (~25 °C) and ambient pressure irradiated by a 300 W Xenon lamp with 420 nm cutoff filter. The power intensity at the central point of the reactant was measured to be 173 mW cm^{-2}. For hydrogen evolution, 50 mg photocatalyst powders were dispersed in 150 mL triethanolamine (TEOA) solution (10 vol%), and H_2PtCl_6 solution equivalent to 3 wt% Pt was added into the suspension. Before light irradiation, the suspensions were purged with argon to remove dissolved air. The amount of hydrogen was measured through online gas chromatography (Shimadzu GC-2014 C) with a thermal conductivity detector (argon carrier gas).

2.4. DFT Calculations

In this study, all the DFT calculation was carried out with the Vienna Ab initio Simulation Package (VASP), projector augmented wave (PAW) method and the Perdew-Burke-Ernzerhof (PBE) function. The electron wave function is expanded by a plane wave with a kinetic energy cutoff of 500 eV. The convergence accuracy of energy values and atomic force were set as 1×10^{-5} eV and 0.02 eV/Å, respectively. A $2 \times 2 \times 1$ Monkhorst-Pack k-point mesh was used to model $In_2O_3/ZnIn_2S_4$. The models of In_2O_3 and $ZnIn_2S_4$ are shown in Fig. S1.

3. Results and discussion

3.1. Preparation and characterization of $In_2O_3/ZnIn_2S_4$ heterostructure

The sandwiched $In_2O_3/ZnIn_2S_4$ heterostructure with layer $ZnIn_2S_4$ were prepared following the progress in Fig. 1a. Firstly, Ca-alginate fibers and indium acetate were chosen as the precursor to obtain In-alginate fibers through an ion exchange method[35]. Scanning electron microscope (SEM) images reveal the rodlike structure of Ca-alginate fibers with smooth surfaces (Fig. S2). The second step is calcination progress to convert In-alginate fibers to In_2O_3 hollow fibers (Fig. 1b and c). The crystallinity can be improved with the increase of calcination temperature, but when the temperature reaches 900 °C, the hollow fibers are destroyed to form fragments (Fig. S3 and S4). Thus, in the following sections, all the In_2O_3 obtained at 800 °C were chosen. Finally, flake-like $ZnIn_2S_4$ layers were loaded onto the outer layer and inner cavity of the In_2O_3 hollow fibers using a chemical bath approach (Fig. 1d). Elemental mappings show Zn, In, O, and S atoms are homogeneously distributed, indicating that $ZnIn_2S_4$ nanosheet growing uniformly on the surface In_2O_3 hollow fibers. $In_2O_3/ZnIn_2S_4$ samples with different amounts of $ZnIn_2S_4$ (labelled $In_2O_3/ZnIn_2S_4$-11.0%, $In_2O_3/ZnIn_2S_4$-5.6%, $In_2O_3/ZnIn_2S_4$-2.8%, respectively) were obtained, and their SEM images are shown in Fig. S5. Among them, $In_2O_3/ZnIn_2S_4$-5.6% shows the highest H_2 evolution rate, thus if there are no special instructions, $In_2O_3/ZnIn_2S_4$ in the article refers to $In_2O_3/ZnIn_2S_4$-5.6%. As for bare $ZnIn_2S_4$, it consists of nanoparticles that easily

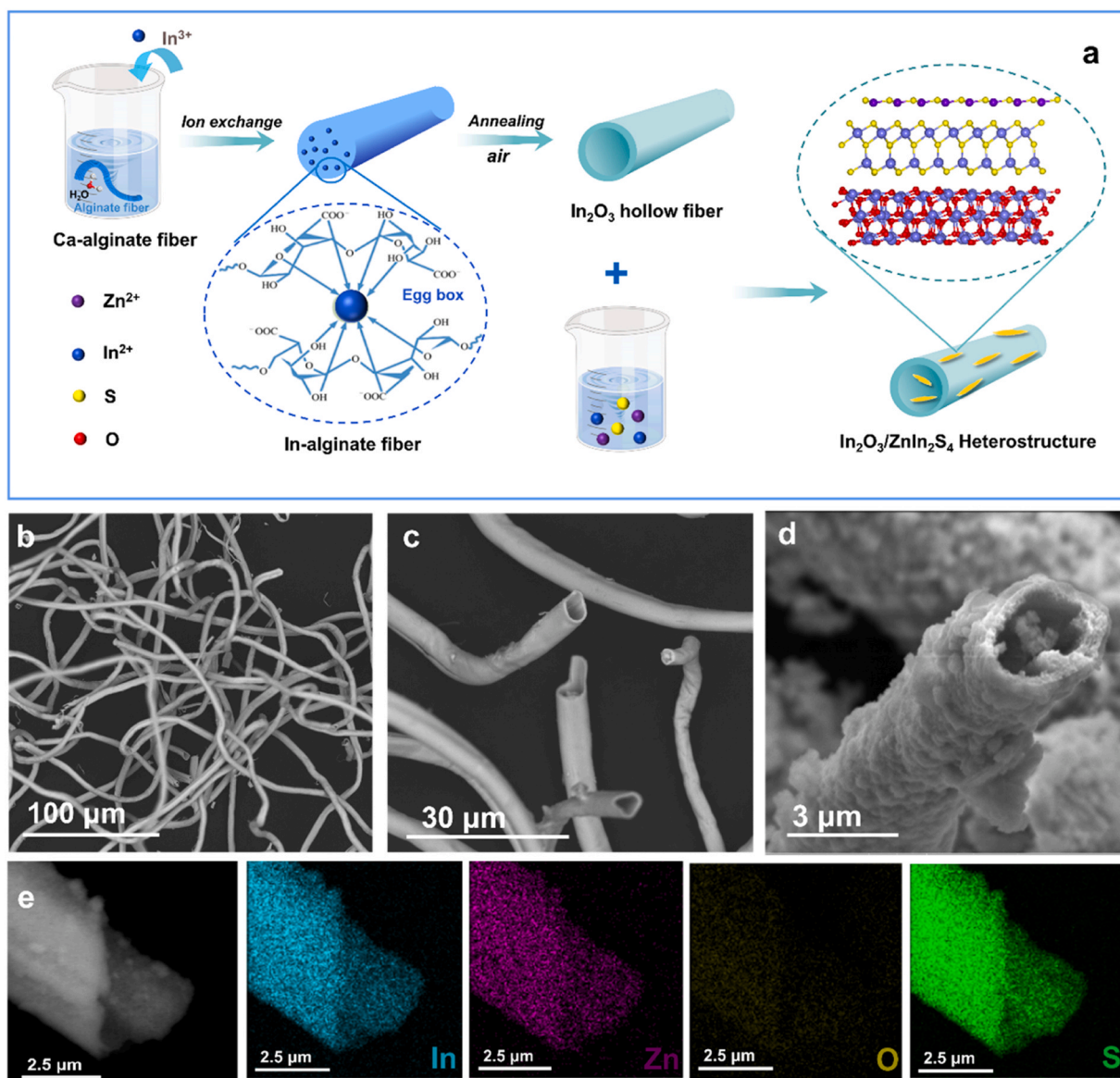**Fig. 1.** (a) Schematic illustration of the synthesis process of the $In_2O_3/ZnIn_2S_4$. SEM images of (b)(c) In_2O_3 calcinated at 800 °C and (d) $In_2O_3/ZnIn_2S_4$. (e) The elements mapping images of the $In_2O_3/ZnIn_2S_4$.

undergo agglomeration (Fig. S6).

X-ray diffraction (XRD) patterns were recorded to probe the phase structure of the as-prepared samples (Fig. 2a). The pristine $ZnIn_2S_4$ shows three diffraction peaks at 21.6°, 27.7°, and 47.2°, which are assigned to the (006), (102), and (110) planes of hexagonal $ZnIn_2S_4$, respectively (JCPDS card no.65–2023) [36,37]. The diffraction peaks of In_2O_3 hollow fibers are well matched with those of standard cubic phase In_2O_3 (JCPDS card no.06–0416)[38,39]. Meanwhile, all the diffraction peaks can be completely ascribed to that of In_2O_3 and $ZnIn_2S_4$, and the characteristic peaks of $ZnIn_2S_4$ become stronger with the increasing amount of $ZnIn_2S_4$ contents. Besides, no other impurity phase is observed, indicating the successful construction of target samples. The sandwich structure consists of In_2O_3 and layered $ZnIn_2S_4$ are displayed in their transmission electron microscope (TEM) images (Fig. 2b) and the high-resolution TEM (HRTEM) images (Fig. 2c), which the two phases matched perfectly to form a stable interface. Inversing fast Fourier transformation (IFFT) images show the lattice fringes with d-spacing of 0.40 nm and 0.29 nm are attributed to the (006) and (014) planes of $ZnIn_2S_4$ (Fig. 2d). Fig. 2e shows the lattice fringes with d-spacing of 0.50 nm and 0.29 nm corresponding to the (200) and (222)

planes of In_2O_3. Notably, as shown in Fig. 2f, the (006) facet of $ZnIn_2S_4$ is parallel to the (222) facet of In_2O_3, indicating the (001) plane of $ZnIn_2S_4$ connects the (222) plane of In_2O_3 to form intimate interface [40]. What's more, computational investigations were conducted to further prove it, and the schematic atomic arrangement of the interface between these two components is displayed in Fig. 2g. When the (222) of In_2O_3 and the (001) of $ZnIn_2S_4$ are combined (In_2O_3: $a=b=14.6$, $c=27.8$, $\alpha = \beta = 90°$, $\gamma = 120°$, $ZnIn_2S_4$: $a=b=15.7$, $c=29.5$, $\alpha = \beta = 90°$, $\gamma = 120°$), the lattice mismatch between (001) plane of $ZnIn_2S_4$ and (222) plane of In_2O_3 is less than 5%, indicating a stable interface established in $In_2O_3/ZnIn_2S_4$. Elemental mappings of $In_2O_3/ZnIn_2S_4$ (Fig. 2g) display the uniform distribution of In, Zn, S and O elements, further proving that $ZnIn_2S_4$ nanosheets were successfully introduced on In_2O_3 hollow fibers.

The specific surface area and pore size distribution of the samples were determined from the N_2 adsorption and desorption isotherms (Fig. S7). All samples can be categorized as type IV isotherms, suggesting that there are micro-mesoporous structures in the catalysts, this coincides with the result of pore size distribution plot. The specific surface area of $ZnIn_2S_4$, In_2O_3, $In_2O_3/ZnIn_2S_4$-5.6% are 223.0, 18.8 and

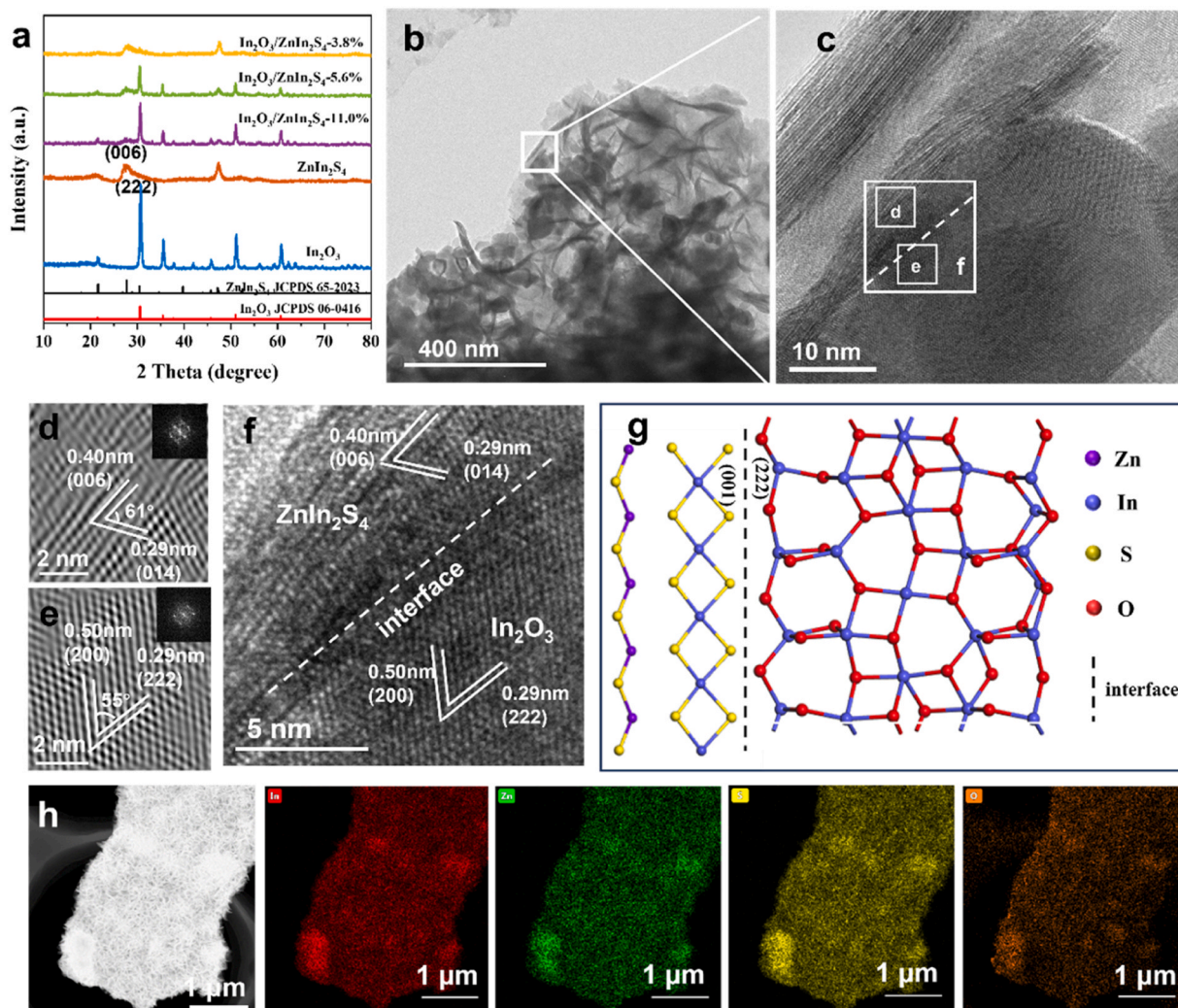**Fig. 2.** (a) XRD patterns of $In_2O_3/ZnIn_2S_4$ with different $ZnIn_2S_4$ concentrations. (b) TEM and (c, f) High-resolution TEM images of $In_2O_3/ZnIn_2S_4$. (d, e) IFFT images of the selected area (Inset: FFT image of the selected area). (g) Schematic atomic arrangement of the interface between In_2O_3 and $ZnIn_2S_4$ phase. (h) Elemental mappings of $In_2O_3/ZnIn_2S_4$.

$55.7 \ m^2/g$. This results indicate that the construction of heterostructure is the main factor affecting the hydrogen production performance of catalysts in this system. Although $In_2O_3/ZnIn_2S_4$ has a smaller specific surface area than $ZnIn_2S_4$, its hydrogen production performance is much higher than that of $ZnIn_2S_4$ due to the formation of heterostructure that greatly accelerate charge separation and transfer (Table S1).

X-ray photoelectron spectroscopy (XPS) was performed to investigate the chemical compositions of In_2O_3, $ZnIn_2S_4$ and $In_2O_3/ZnIn_2S_4$ samples. The wide-scan survey XPS spectrum of $In_2O_3/ZnIn_2S_4$ shows the expected elements of S, In, Zn, and O (Fig. S8). The In 3d high-resolution XPS spectrum (Fig. 3a) of $In_2O_3/ZnIn_2S_4$ exhibits two prominent peaks at 444.8 eV and 452.4 eV, which can be assigned to In $3d_{5/2}$ and In $3d_{3/2}$ of In^{3+}, respectively[41–43]. For the Zn 2p spectra (Fig. 3b), the two peaks with binding energies of 1021.8 and 1044.8 eV corresponded to Zn $2p_{3/2}$ and Zn $2p_{1/2}$, respectively, which is in good agreement with the values for Zn^{2+} [44,45]. As shown in Fig. 3c, the O 1 s spectrum can be divided into two peaks located at 530.0 and 531.4 eV, which can be attributed to lattice oxygen in In–O–In bond (O_L) and oxygen vacancy (O_v) in the metal oxide support, respectively[46, 47]. Compared with $In_2O_3/ZnIn_2S_4$, In_2O_3 exhibits a larger peak area of O_v, suggesting that the concentration of O_v decreased after loading $ZnIn_2S_4$. In consistent with the XPS analyses, the enhanced electron spin resonance (EPR) peak intensity demonstrated more O_v in In_2O_3 than

$In_2O_3/ZnIn_2S_4$ (Fig. S9), indicating the loading of $ZnIn_2S_4$ reduces O_v and the recombination centers of electron holes. This could suppress the recombination of photogenerated electrons and holes. Notably, the S 2p high-resolution XPS spectrum (Fig. 3d) splits into $2p_{3/2}$ (161.7 eV) and $2p_{1/2}$ (162.9 eV) peaks, which can be ascribed to S^{2-} ions[48,49]. It is worth noting that the peaks of Zn 2p and S 2p for $In_2O_3/ZnIn_2S_4$ are observed to shift towards higher energy, as compared to those in $ZnIn_2S_4$. Conversely, the peak of O 1 s was observed to shift towards lower energy as compared to that in In_2O_3. These observations suggest that the electron transfer from $ZnIn_2S_4$ to In_2O_3 in the $In_2O_3/ZnIn_2S_4$ composites.

3.2. Photocatalytic activity for H_2 evolution

HER activities under visible light irradiation were evaluated and shown in Fig. 4a and b. TEOA was used as a sacrificial agent to react with holes to generate $TEOA^+$ during the reaction process, and thus inhibited the recombination of electrons and holes. In addition, H_2PtCl_6 was added to produce Pt as co-catalyst to improve the photocatalytic HER activity. The pure In_2O_3 hollow fibers sample shows no HER performance, while $ZnIn_2S_4$ exhibited very weak HER activity (0.63 mmol/g/h). The $In_2O_3/ZnIn_2S_4$ samples display a volcano-type curve of H_2 evolution rates depending on the $ZnIn_2S_4$ contents, and $In_2O_3/ZnIn_2S_4$-

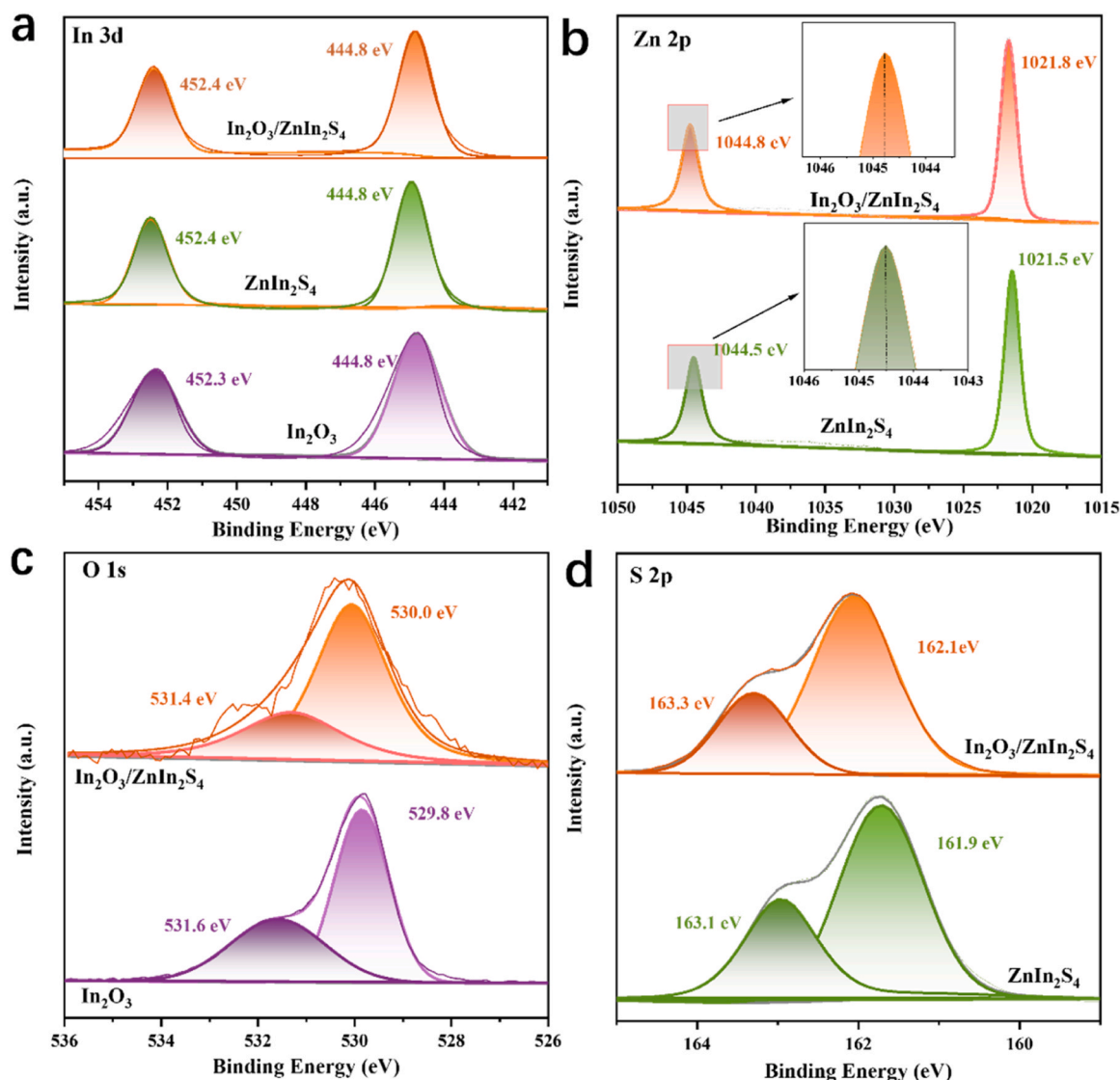**Fig. 3.** High-resolution XPS spectra of (a) In 3d, (b) Zn 2p, (c) O 1 s, and (d) S 2p spectra of In_2O_3, $ZnIn_2S_4$ and $In_2O_3/ZnIn_2S_4$.
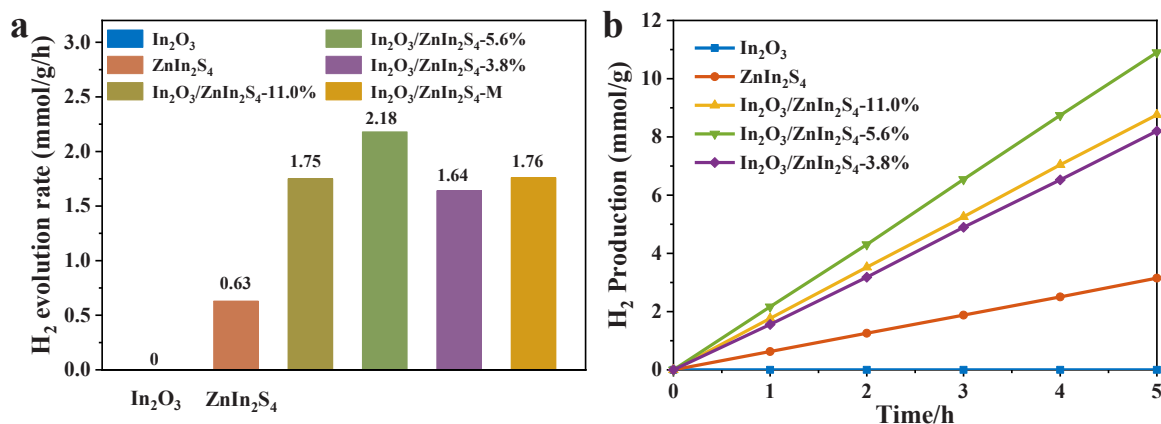

Fig. 4. (a) Photocatalytic HER performances of different samples. (b) Time−yield plots of HER of different samples.

5.6% shows the highest HER rate reaching to 2.18 mmol/g/h. In order to prove the superior activity of the heterostructure, we used a grinding method to mechanically mix $ZnIn_2S_4$ and In_2O_3 to obtain $In_2O_3/ZnIn_2S_4$-M, which exhibited significantly lower hydrogen production performance (1.76 mmol/g/h) than $In_2O_3/ZnIn_2S_4$ prepared by in-situ methods (2.18 mmol/g/h). The literature survey of the photocatalytic activity reported for other In_2O_3-based catalysts is summarized in Table S2, and the HER activities reported for these In_2O_3 materials are

much lower than that achieved for In$_2$O$_3$/ZnIn$_2$S$_4$ in the present works. Cycling experiments were conducted to prove the stability of the sample (Fig. S10). Besides, the SEM images (Fig. S11) and XRD patterns (Fig. S12) prove that no significant structure changes of In$_2$O$_3$/ZnIn$_2$S$_4$ are observed during the H$_2$ evolution process, indicating good stability of In$_2$O$_3$/ZnIn$_2$S$_4$. Specifically, the In$_2$O$_3$/ZnIn$_2$S$_4$ heterostructure depicts an apparent quantum efficiency (AQE) value of 15.9% at 420 nm (Table S3).

Photoelectrochemical experiments were employed to investigate the photocatalytic HER activity enhancement mechanism over In$_2$O$_3$/ZnIn$_2$S$_4$, which the highest transient photocurrent of In$_2$O$_3$/ZnIn$_2$S$_4$-5.6% proved faster charge separation compared with other samples (Fig. 5a)[50,51]. Electrochemical impedance spectroscopy (EIS) showed In$_2$O$_3$/ZnIn$_2$S$_4$ possess smaller interfacial resistance and In$_2$O$_3$/ZnIn$_2$S$_4$-5.6% is the smallest (Fig. 5b), thus the charge transfer in this sample is faster [52–54]. The lowest photoluminescence (PL) emission response also confirmed the excellent charge separation efficiency of In$_2$O$_3$/ZnIn$_2$S$_4$-5.6% (Fig. 5c)[55–57]. Furthermore, EPR was conducted to detect active species generated during the HER progress. 2,2,6,6-Tetramethylpiperidinooxy (TEMPO) can generate strong EPR signals due to its paramagnetism. It can be seen that all samples have strong signal peaks under dark conditions, indicating the presence of TEMPO. Under illumination, the signal peaks of all three samples decreased, indicating h$^+$ was produced, which reacted with TEMPO to form TEMPO$^+$. The signal peak of the In$_2$O$_3$/ZnIn$_2$S$_4$ sample decreased most after irradiation, and almost no TEMPO signal peak can be observed, indicating the electrons and holes in In$_2$O$_3$/ZnIn$_2$S$_4$ sample were most numerous. This indicates that the construction of heterostructure accelerates the separation and transfer of electrons-holes, thereby improving the performance of photocatalytic hydrogen production (Fig. 5d-f).

UV–vis diffuse reflectance spectroscopy was used to investigate the optical properties of different samples. Pure In$_2$O$_3$ and ZnIn$_2$S$_4$ possess absorption band edges of 476 and 487 nm. Compared to the In$_2$O$_3$ hollow fiber, all the In$_2$O$_3$/ZnIn$_2$S$_4$ samples possessed a broad absorption in the visible light region, with the absorption edge red-shifted. With the increase of ZnIn$_2$S$_4$ amounts, the redshift of the absorption edge is more obvious (Fig. 6a). The optical absorption indicated that the hybridization of In$_2$O$_3$ with ZnIn$_2$S$_4$ can greatly improve the optical absorption ability to harvest visible light, thus contributing to the photocatalytic enhancement in the visible-light region. The bandgaps of In$_2$O$_3$ and ZnIn$_2$S$_4$ determined from a plot of $(\alpha h\nu)^2$ versus $h\nu$, were about 2.35 and 2.78 eV (Fig. 6b) [36,58].

Referring to the Mott-Schottky plots, the flat band potential of In$_2$O$_3$ and ZnIn$_2$S$_4$ are determined in Fig. 6c, considering that the flat band potential (V$_{fb}$) of n-type semiconductor is usually ~0.2 V more positive than the CB, the CB positions of In$_2$O$_3$ and ZnIn$_2$S$_4$ could be determined as − 0.75 and − 0.94 (vs NHE), respectively [59,60]. Accordingly, the VB position of In$_2$O$_3$ and ZnIn$_2$S$_4$ were estimated to be 2.03 and 1.41 V (vs. NHE), consistent with the values calculated from XPS valence spectra results (Fig. 6d).

3.3. DFT calculations

Fig. 7a shows the calculated work functions (W$_F$) of ZnIn$_2$S$_4$ and In$_2$O$_3$, which are 4.23 and 4.64 eV, respectively, thus leading to the charge transfer from ZnIn$_2$S$_4$ to In$_2$O$_3$ to reach the Femi level equilibrium. Similar results can be obtained from the charge density difference (Fig. 7b). Blue and orange parts represent the depletion and accumulation of electrons, respectively. The redistribution of electron density for In$_2$O$_3$/ZnIn$_2$S$_4$, with electron depletion mainly on the ZnIn$_2$S$_4$ surface and electron accumulation on In$_2$O$_3$, suggests that the In$_2$O$_3$ side of the In$_2$O$_3$/ZnIn$_2$S$_4$ heterostructure has the strong ability to enrich electrons [61,62].

Based on above discussion, the photocatalytic H$_2$ production mechanism was proposed in Fig. 7c. A tightly heterostructure was successfully formed between the In$_2$O$_3$ hollow fibers and the ZnIn$_2$S$_4$ due to the higher lattice matching degree. Thus, under visible light irradiation, the electrons will transfer from ZnIn$_2$S$_4$ to In$_2$O$_3$, and the holes transfer to the opposite direction through tightly-bound interface. This leads to the effective separation of photogenerated electrons and holes, thus inhibiting their recombination, which greatly enhances the photocatalytic hydrogen production activity.
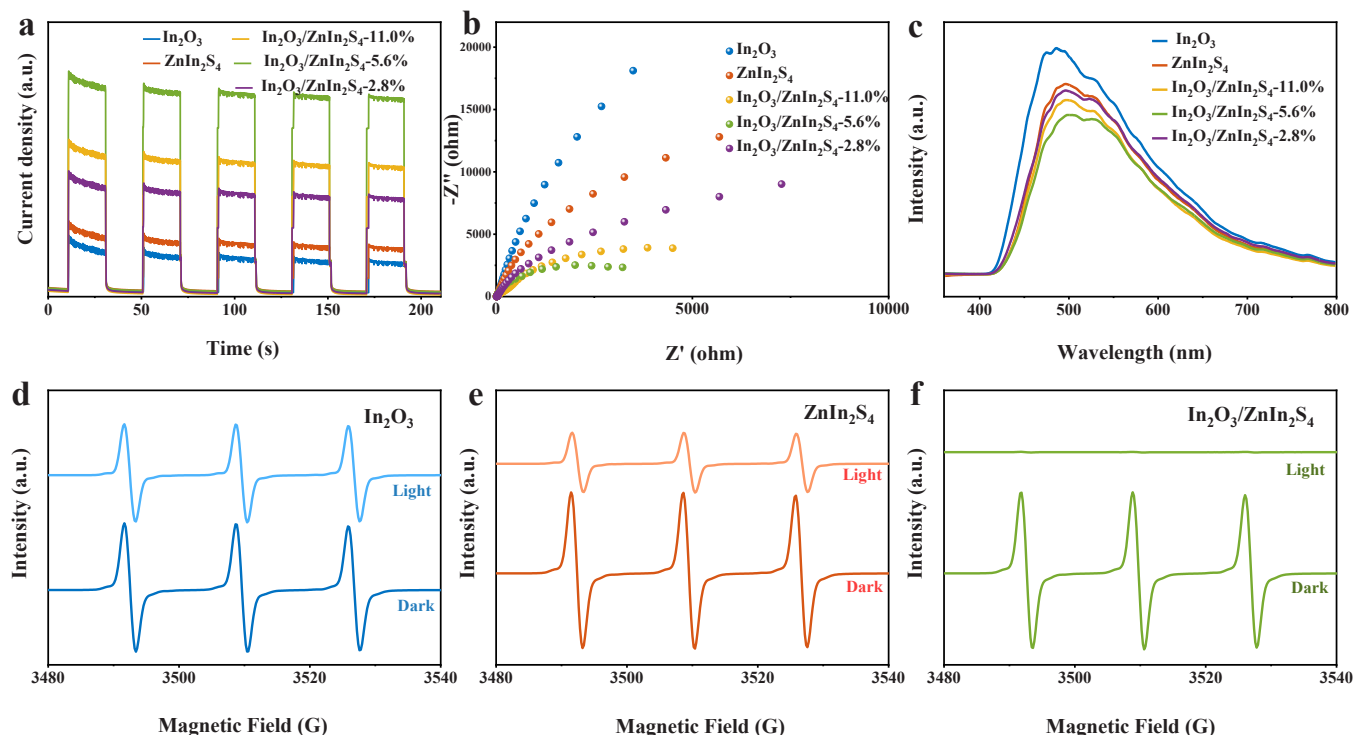
Fig. 5. (a) Transient photocurrent curves, (b) EIS plots, (c) PL spectra and (d-f) EPR spectra of TEMPO-h$^+$ adducts of In$_2$O$_3$, ZnIn$_2$S$_4$ and In$_2$O$_3$/ZnIn$_2$S$_4$.
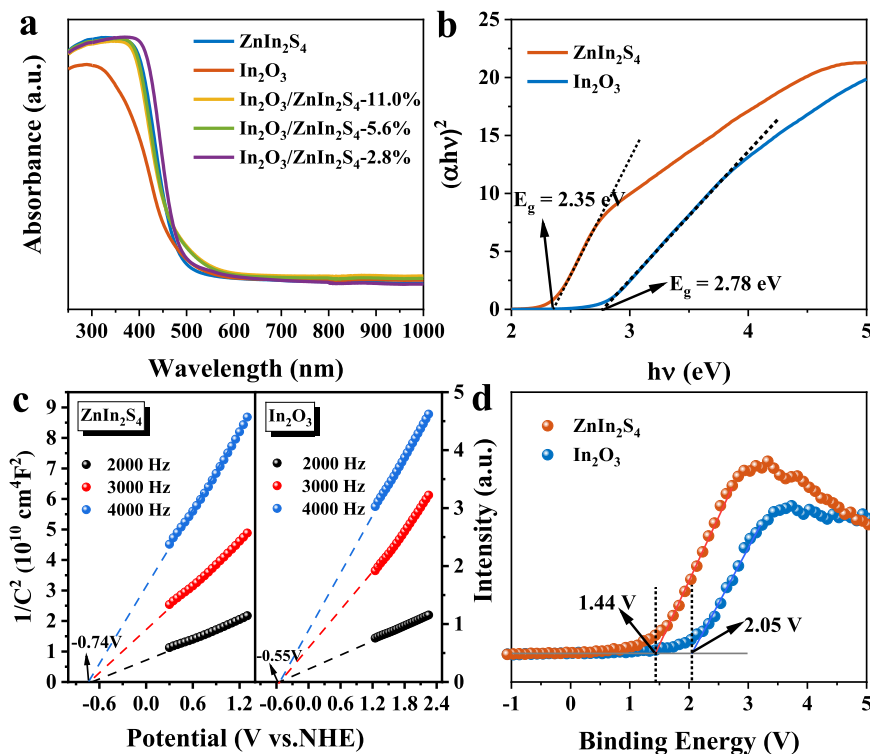
Fig. 6. (a) UV–vis diffuse reflectance spectroscopy of different samples. (b) Plots of $(\alpha h\nu)^2$ vs. $h\nu$ for In_2O_3 and $ZnIn_2S_4$. (c) Mott–Schottky plots and (d) XPS valence spectra of In_2O_3 and $ZnIn_2S_4$.
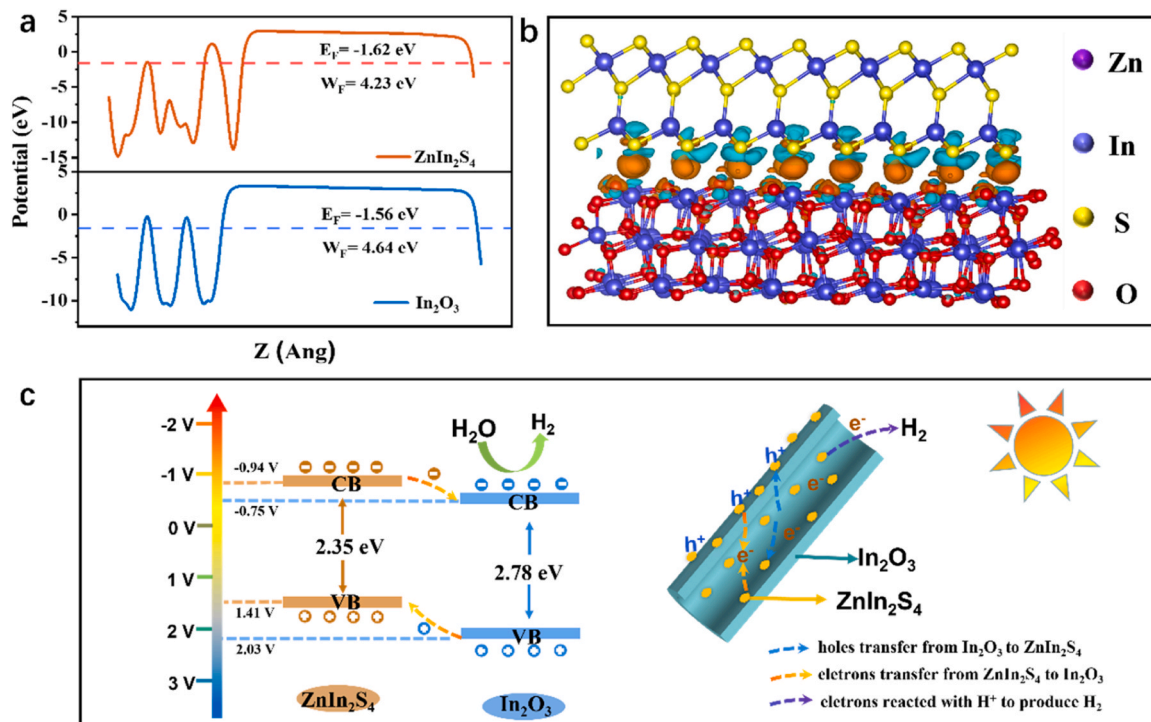

Fig. 7. (a) Work functions of In_2O_3 and $ZnIn_2S_4$. (b) Charge density difference at $ZnIn_2S_4(001)/In_2O_3(222)$ interface. (c) Proposed mechanism of HER in the $In_2O_3/ZnIn_2S_4$ system.

4. Conclusion

In this study, we successfully fabricated a novel $In_2O_3/ZnIn_2S_4$ sandwich heterostructure, which exhibited a significant enhancement in photocatalytic activity for hydrogen production. By optimizing the $ZnIn_2S_4$ loading, the $In_2O_3/ZnIn_2S_4$ heterostructure achieved an impressive photocatalytic HER rate of 2.18 mmol/g/h under visible light irradiation, which is much higher than pure In_2O_3 and $ZnIn_2S_4$.

Tightly-bound heterostructure between $In_2O_3(222)$ and $ZnIn_2S_4(001)$ was successfully constructed attributed to the high degree of lattice matching between In_2O_3 and $ZnIn_2S_4$, facilitating efficient charge transfer and resulting in outstanding hydrogen production performance. This work introduces new insights into the atomic-level design and construction of heterostructures, offering a promising direction for further advancements in heterostructure research.

CRediT authorship contribution statement

Wang Xiaoxia: Conceptualization, Software. **Liu Yan:** Data curation, Formal analysis. **Ji Zhilin:** Methodology. **Yang Dongjiang:** Funding acquisition, Methodology, Resources, Writing – review & editing. **Jiang Luhua:** Methodology, Resources, Writing – review & editing. **Hui Bin:** Validation. **Zhu Yukun:** Funding acquisition, Methodology. **Lu Ping:** Conceptualization, Investigation, Methodology, Writing – original draft. **Liu Ke:** Methodology, Writing – review & editing.

Declaration of Competing Interest

The authors declare that they have no known competing financial interests or personal relationships that could have appeared to influence the work reported in this paper.

Data Availability

No data was used for the research described in the article.

Acknowledgments

Appendix A. Supporting information

Supplementary data associated with this article can be found in the online version at doi:10.1016/j.apcatb.2024.123697.

References

[1] S. Liu, Z. Tang, Y. Sun, J. Colmenares, Y. Xu, One-dimension-based spatially ordered architectures for solar energy conversion, Chem. Soc. Rev. 44 (2015) 5053–5075, https://doi.org/10.1039/c4cs00408f.

[2] E. Pena, J. Becerra, V. Gopalakrishnan, T. Do, Facile one-pot synthesis of plasmonic gold nanoparticles decorated porphyrin-metal organic framework for photocatalytic hydrogen evolution, Mol. Catal. 548 (2023) 113470, https://doi.org/10.1016/j.mcat.2023.113470.

[3] M. Qi, M. Conte, M. Anpo, Z. Tang, Y. Xu, Cooperative coupling of oxidative organic synthesis and hydrogen production over semiconductor-based photocatalysts, Chem. Rev. 121 (2021) 13051–13085, https://doi.org/10.1021/acs.chemrev.1c00197.

[4] T. Song, J. Wang, L. Su, H. Xu, X. Bai, L. Zhou, W. Tu, Promotion effect of rhenium on $MoS_2/ReS_2@CdS$ nanostructures for photocatalytic hydrogen production, Mol. Catal. 516 (2021) 111939, https://doi.org/10.1016/j.mcat.2021.111939.

[5] B. Yan, H. Song, G. Yang, A facile and green large-scale fabrication of single atom catalysts for high photocatalytic H_2 evolution activity, Chem. Eng. J. 427 (2022) 131795, https://doi.org/10.1016/j.cej.2021.131795.

[6] R. Asahi, T. Morikawa, T. Ohwaki, K. Aoki, Y. Taga, Visible-light photocatalysis in nitrogen-doped titanium oxides, Science 293 (2001) 269–271, https://doi.org/10.1126/science.1061051.

[7] B. Han, S. Liu, N. Zhang, Y. Xu, Z. Tang, One-dimensional $CdS@MoS_2$ core-shell nanowires for boosted photocatalytic hydrogen evolution under visible light, Appl. Catal. B: Environ. 202 (2017) 298–304, https://doi.org/10.1016/j.apcatb.2016.09.023.

[8] Y. Li, M. Qi, J. Li, Z. Tang, Y. Xu, Noble metal free $CdS@CuS-NixP$ hybrid with modulated charge transfer for enhanced photocatalytic performance, Appl. Catal. B: Environ. 257 (2019) 117934, https://doi.org/10.1016/j.apcatb.2019.117934.

[9] K. Lu, M. Qi, Z. Tang, Y. Xu, Earth-abundant MoS_2 and cobalt phosphate dual cocatalysts on 1D CdS nanowires for boosting photocatalytic hydrogen production, Langmuir 35 (2019) 11056–11065, https://doi.org/10.1021/acs.langmuir.9b01409.

[10] W. Wang, X. Bai, Q. Ci, L. Du, X. Ren, D. Phillips, Near-field drives long-lived shallow trapping of polymeric C_3N_4 for efficient photocatalytic hydrogen evolution, Adv. Funct. Mater. 31 (2021) 2103978, https://doi.org/10.1002/adfm.202103978.

[11] Y. Deng, H. Zhou, Y. Zhao, B. Yang, M. Shi, X. Tao, S. Yang, R. Li, C. Li, Spatial separation of photogenerated charges on well-defined bismuth vanadate square nanocrystals, Small 18 (2021) 2103245.

[12] G. Liu, J. Pan, L. Yin, J. Irvine, F. Li, J. Tan, P. Wormald, H. Cheng, Heteroatom-modulated switching of photocatalytic hydrogen and oxygen evolution preferences of anatase TiO_2 microspheres, Adv. Funct. Mater. 22 (2012) 3233–3238, https://doi.org/10.1002/adfm.201200414.

[13] J. Wang, C. Liu, T. Senftle, J. Zhu, G. Zhang, X. Guo, C. Song, Variation in the In_2O_3 crystal phase alters catalytic performance toward the reverse water gas shift reaction, ACS Catal. 10 (2019) 3264–3273, https://doi.org/10.1021/acscatal.9b04239.

[14] Z. Wang, L. Wang, Role of oxygen vacancy in metal oxide based photoelectrochemical water splitting, EcoMat 3 (2021) 12075, https://doi.org/10.1002/eom2.12075.

[15] Z. Jin, Y. Liu, X. Hao, Self-assembly of zinc cadmium sulfide nanorods into nanoflowers with enhanced photocatalytic hydrogen production activity, J. Colloid Interface Sci. 567 (2020) 357–368, https://doi.org/10.1016/j.jcis.2020.02.024.

[16] P. Zhang, T. Wang, X. Chang, L. Zhang, J. Gong, Synergistic cocatalytic effect of carbon nanodots and Co_3O_4 nanoclusters for the photoelectrochemical water oxidation on hematite, Angew. Chem. Int. Ed. 55 (2016) 5851–5855, https://doi.org/10.1002/anie.201600918.

[17] Y. Yang, J. Wu, B. Cheng, L. Zhang, A. Al-Ghamdi, S. Wageh, Y. Li, Enhanced photocatalytic H_2-production activity of CdS nanoflower using single atom pt and graphene quantum dot as dual cocatalysts, Chin. J. Struct. Chem. 41 (2022) 2206006–2206014.

[18] J. Zou, G. Liao, J. Jiang, Z. Xiong, S. Bai, H. Wang, P. Wu, P. Zhang, X. Li, In-situ Construction of sulfur-doped $g-C_3N_4$/defective $g-C_3N_4$ iso-type step-scheme heterojunction for boosting photocatalytic H_2 evolution, Chin. J. Struct. Chem. 41 (2022) 2201025–2201033.

[19] J. Tang, R. Wang, M. Liu, Z. Zhang, Y. Song, S. Xue, Z. Zhao, D. Dionysiou, Construction of novel Z-scheme $Ag/FeTiO_3/Ag/BiFeO_3$ photocatalyst with enhanced visible-light-driven photocatalytic performance for degradation of norfloxacin, Chem. Eng. J. 351 (2018) 1056–1066, https://doi.org/10.1016/j.cej.2018.06.171.

[20] Q. Zhang, S. Huang, J. Deng, D. Gangadharan, F. Yang, Z. Xu, G. Giorgi, M. Palummo, M. Chaker, D. Ma, Ice-assisted synthesis of black phosphorus nanosheets as a metal-free photocatalyst: 2D/2D heterostructure for broadband H_2 evolution, Adv. Funct. Mater. 29 (2019) 1902486, https://doi.org/10.1002/adfm.201902486.

[21] M. Tan, Y. Ma, C. Yu, Q. Luan, J. Li, C. Liu, W. Dong, Y. Su, L. Qiao, L. Gao, Q. Lu, Y. Bai, Boosting photocatalytic hydrogen production via interfacial engineering on 2d ultrathin Z-scheme $ZnIn_2S_4/g-C_3N_4$ heterojunction, Adv. Funct. Mater. 32 (2021) 2111740, https://doi.org/10.1002/adfm.202111740.

[22] L.C. Tien, J.L. Shih, Type-II $\alpha-In_2S_3/In_2O_3$ nanowire heterostructures: evidence of enhanced photo-induced charge separation efficiency, RSC Adv. 6 (2016) 12561–12570, https://doi.org/10.1039/c5ra24370j.

[23] X. Liu, L. Zhang, Y. Li, X. Xu, Y. Du, Y. Jiang, K. Lin, A novel heterostructure coupling MOF-derived fluffy porous indium oxide with $g-C_3N_4$ for enhanced photocatalytic activity, Mater. Res. Bull. 133 (2021) 111078, https://doi.org/10.1016/j.materresbull.2020.111078.

[24] J. Ren, K. Yuan, K. Wu, L. Zhou, Y. Zhang, A robust CdS/In_2O_3 hierarchical heterostructure derived from a metal–organic framework for efficient visible-light photocatalytic hydrogen production, Inorg. Chem. Front. 6 (2019) 366–375, https://doi.org/10.1039/c8qi01202d.

[25] S. Liu, F. Li, Y. Li, Y. Hao, X. Wang, B. Li, R. Liu, Fabrication of ternary $g-C_3N_4$/Al_2O_3/ZnO heterojunctions based on cascade electron transfer toward molecular oxygen activation, Appl. Catal. B: Environ. 212 (2017) 115–128, https://doi.org/10.1016/j.apcatb.2017.04.072.

[26] Z. Li, M. Jia, S. Doble, E. Hockey, H. Yan, J. Avenoso, D. Bodine, Y. Zhang, C. Ni, J. Newberg, L. Gundlach, energy band architecture of a hierarchical $ZnO/Au/Cu_xO$ nanoforest by mimicking natural superhydrophobic surfaces, ACS Appl. Mater. Interfaces 11 (2019) 40490–40502, https://doi.org/10.1021/acsami.9b13610.

[27] Y. Qin, H. Li, J. Lu, Y. Feng, F. Meng, C. Ma, Y. Yan, M. Meng, Synergy between van der waals heterojunction and vacancy in $ZnIn_2S_4/g-C_3N_4$ 2D/2D photocatalysts for enhanced photocatalytic hydrogen evolution, Appl. Catal. B: Environ. 277 (2020) 119254, https://doi.org/10.1016/j.apcatb.2020.119254.

[28] J. Du, H. Shi, J. Wu, K. Li, C. Song, X. Guo, Interface and defect engineering of a hollow $TiO_2@ZnIn_2S_4$ heterojunction for highly enhanced CO_2 photoreduction activity, ACS Sustain. Chem. Eng. 11 (2023) 2531–2540, https://doi.org/10.1021/acssuschemeng.2c06693.

[29] Z. Guan, J. Pan, Q. Li, G. Li, J. Yang, Boosting visible-light photocatalytic hydrogen evolution with an efficient $CuInS_2/ZnIn_2S_4$ 2D/2D heterojunction, ACS Sustain. Chem. Eng. 7 (2019) 7736–7742, https://doi.org/10.1021/acssuschemeng.8b06587.

[30] C. Du, B. Yan, G. Yang, Self-integrated effects of 2D $ZnIn_2S_4$ and amorphous Mo_2C nanoparticles composite for promoting solar hydrogen generation, Nano Energy 76 (2020) 105031, https://doi.org/10.1016/j.nanoen.2020.105031.

[31] Y. Chao, P. Zhou, N. Li, J. Lai, Y. Yang, Y. Zhang, Y. Tang, W. Yang, Y. Du, D. Su, Y. Tan, S. Guo, Ultrathin visible-light-driven mo incorporating In₂O₃–ZnIn₂S₄ Z-scheme nanosheet photocatalysts, Adv. Mater. 31 (2018) 5037, https://doi.org/10.1002/adma.201807226.

[32] S. Wang, B. Guan, X. Lou, Construction of ZnIn₂S₄-In₂O₃ hierarchical tubular heterostructures for efficient co₂ photoreduction, J. Am. Chem. Soc. 140 (2018) 5037–5040, https://doi.org/10.1021/jacs.8b02200.

[33] S. Wang, B. Guan, X. Wang, X. Lou, Formation of hierarchical Co₉S₈@ZnIn₂S₄ heterostructured cages as an efficient photocatalyst for hydrogen evolution, J. Am. Chem. Soc. 140 (2018) 15145–15148, https://doi.org/10.1021/jacs.8b07721.

[34] Z. Xiong, Y. Hou, R. Yuan, Z. Ding, W. Ong, S. Wang, Hollow NiCo₂S₄ nanospheres as a cocatalyst to support ZnIn₂S₄ nanosheets for visible-light-driven hydrogen production, Acta Phys. Chim. Sin. 0 (2021), https://doi.org/10.3866/PKU.WHXB202111021.

[35] C. Lv, H. Liu, D. Li, S. Chen, H. Zhang, X. She, X. Guo, D. Yang, Ultrafine FeSe nanoparticles embedded into 3D carbon nanofiber aerogels with FeSe/Carbon interface for efficient and long-life sodium storage, Carbon 143 (2019) 106–115, https://doi.org/10.1016/j.carbon.2018.10.091.

[36] Y. Wang, X. Kong, M. Jiang, F. Zhang, X. Lei, A Z-scheme ZnIn₂S₄/Nb₂O₅ nanocomposite: constructed and used as an efficient bifunctional photocatalyst for H₂ evolution and oxidation of 5-hydroxymethylfurfural, Inorg. Chem. Front. 7 (2020) 437–446, https://doi.org/10.1039/c9qi01196j.

[37] Q. Liang, W. Gao, C. Liu, S. Xu, Z. Li, A novel 2D/1D core-shell heterostructures coupling MOF-derived iron oxides with ZnIn₂S₄ for enhanced photocatalytic activity, J. Hazard. Mater. 392 (2020) 122500, https://doi.org/10.1016/j.jhazmat.2020.122500.

[38] D. Zhang, Y. Cao, Z. Yang, J. Wu, Nanoheterostructure construction and DFT study of Ni-doped In₂O₃ nanocubes/WS₂ hexagon nanosheets for formaldehyde sensing at room temperature, ACS Appl. Mater. Interfaces 12 (2020) 11979–11989, https://doi.org/10.1021/acsami.9b15200.

[39] W. Wang, X. Wang, S. Wang, J. Yan, Q. Ge, C. Liu, Reverse water gas shift over In₂O₃–CeO₂ catalysts, Catal. Today 259 (2016) 402–408, https://doi.org/10.1016/j.cattod.2015.04.032.

[40] H. Liu, Z. Zheng, D. Yang, X. Ke, E. Jaatinen, J. Zhao, H. Zhu, Coherent interfaces between crystals innanocrystal composites, ACS Nano 4 (2010) 6219–6227, https://doi.org/10.1021/nn101708q.

[41] J. Zhang, Z. Pan, Y. Yang, P. Wang, C. Pei, W. Chen, G. Huang, Boosting the catalytic activity of a step-scheme In₂O₃/ZnIn₂S₄ hybrid system for the photofixation of nitrogen, Chin. J. Catal. 43 (2022) 265–275, https://doi.org/10.1016/s1872-2067(21)63801-9.

[42] J. Ding, Z. Zheng, H. Gao, S. Wang, S. Wu, S. Fang, F. Cheng, Operando non-topological conversion constructing the high-performance nickel-zinc battery anode, Biochem. Eng. J. 414 (2021) 128716, https://doi.org/10.1016/j.cej.2021.128716.

[43] Q. Chen, X. Chen, Q. Jiang, Z. Zheng, Z. Song, Z. Zhao, Z. Xie, Q. Kuang, Constructing oxide/sulfide in-plane heterojunctions with enlarged internal electric field for efficient CO₂ photoreduction, Appl. Catal. B: Environ. 297 (2021) 120394, https://doi.org/10.1016/j.apcatb.2021.120394.

[44] Q. Zhang, J. Zhang, X. Wang, L. Li, Y. Li, W. Dai, In–N–In Sites boosting interfacial charge transfer in carbon-coated hollow tubular In₂O₃/ZnIn₂S₄ heterostructure derived from In-MOF for enhanced photocatalytic hydrogen evolution, ACS Catal. 11 (2021) 6276–6289, https://doi.org/10.1021/acscatal.0c05520.

[45] X. Zou, C. Yuan, Y. Cui, Y. Dong, D. Chen, H. Ge, J. Ke, Construction of zinc-indium-sulfide/indium oxide step-scheme junction catalyst for enhanced photocatalytic activities of pollutant degradation and hydrogen generation, Sep. Purif. Technol. 266 (2021) 118545, https://doi.org/10.1016/j.seppur.2021.118545.

[46] G. Zhuang, Q. Fang, J. Wei, C. Yang, M. Chen, Z. Lyu, Z. Zhuang, Y. Yu, Branched In₂O₃ mesocrystal of ordered architecture derived from the oriented alignment of a metal-organic framework for accelerated hydrogen evolution over In₂O₃-ZnIn₂S₄, ACS Appl. Mater. Interfaces 13 (2021) 9804–9813, https://doi.org/10.1021/acsami.0c19806.

[47] P. Li, T. Liang, H. Liu, J. Li, S. Duo, X. Xu, L. Qiu, X. Wen, R. Shi, In₂O₃ microspheres decorated with ZnIn₂S₄ nanosheets as core-shell hybrids for boosting visible-light photodegradation of organic dyes, Mater. Express 8 (2021) 025505, https://doi.org/10.1088/2053-1591/abe2e2.

[48] M. Wang, G. Zhang, Z. Guan, J. Yang, Q. Li, Spatially separating redox centers and photothermal effect synergistically boosting the photocatalytic hydrogen evolution of ZnIn₂S₄ nanosheets, Small 17 (2021) 2006952, https://doi.org/10.1002/smll.202006952.

[49] R. Bariki, K. Das, S. Pradhan, B. Prusti, B. Mishra, MOF-derived hollow tubular In₂O₃/MIIIn₂S₄ (MII: Ca, Mn, and Zn) heterostructures: synergetic charge-transfer mechanism and excellent photocatalytic performance to boost activation of small atmospheric molecules, ACS Appl. Energy Mater. 5 (2022) 11002–11017, https://doi.org/10.1021/acsaem.2c01670.

[50] X. Wang, Y. Zhang, J. Li, G. Liu, M. Gao, S. Ren, B. Liu, L. Zhang, G. Han, J. Yu, H. Zhao, F. Rosei, Platinum cluster/carbon quantum dots derived graphene heterostructured carbon nanofibers for efficient and durable solar-driven electrochemical hydrogen evolution, Small Methods 6 (2022) 2101470, https://doi.org/10.1002/smtd.202101470.

[51] Y. Zhu, C. Lv, Z. Yin, J. Ren, X. Yang, C. Dong, H. Liu, R. Cai, Y. Huang, W. Theis, S. Shen, D. Yang, A [001]-oriented Hittorf`s phosphorus nanorods/polymeric carbon nitride heterostructure for boosting wide-spectrum-responsive photocatalytic hydrogen evolution from pure water, Angew. Chem. Int. Ed. 59 (2022) 868–873, https://doi.org/10.1002/anie.201911503.

[52] G. Mao, H. Wu, T. Qiu, D. Bao, L. Lai, W. Tu, Q. Liu, WO₃@Fe₂O₃ core-shell heterojunction photoanodes for efficient photoelectrochemical water splitting, Chin. J. Struct. Chem. 41 (2021) 2208025–2208030.

[53] S. Meng, H. Wu, Y. Cui, X. Zheng, H. Wang, S. Chen, Y. Wang, X. Fu, One-step synthesis of 2D/²D–³D NiS/Zn₃In₂S₆ hierarchical structure toward solar-to-chemical energy transformation of biomass-relevant alcohols, Appl. Catal. B: Environ. 266 (2020) 118617, https://doi.org/10.1016/j.apcatb.2020.118617.

[54] B. Yan, B. He, G. Yang, Nanoscale self-wetting driven monatomization of Ag nanoparticle for excellent photocatalytic hydrogen evolution, Small 18 (2022) 2107840, https://doi.org/10.1002/smll.202107840.

[55] X. Wang, Y. Han, W. Li, J. Li, S. Ren, M. Wang, G. Han, J. Yu, Y. Zhang, H. Zhao, Doped carbon dots enable highly efficient multiple-color room temperature phosphorescence, Adv. Opt. Mater. (2023) 2301962, https://doi.org/10.1002/adom.202301962.

[56] Y. Cao, H. Gou, P. Zhu, Z. Jin, Ingenious design of CoAl-LDH p-n heterojunction based on CuI as holes receptor for photocatalytic hydrogen evolution, Chin. J. Struct. Chem. 41 (2022) 2206079–2206085.

[57] K. Liu, S. Yang, W. Li, Y. Wang, C. Sun, L. Peng, H. Garcia, Non-noble-metal NiS promoted charge separation and photocatalytic hydrogen evolution for ZnCdS nano-islands on spherical SiO₂, Fuel 337 (2023) 126840, https://doi.org/10.1016/j.fuel.2022.126840.

[58] G. Wang, R. Huang, J. Zhang, J. Mao, D. Wang, Y. Li, Synergistic modulation of the separation of photo-generated carriers via engineering of dual atomic sites for promoting photocatalytic performance, Adv. Mater. 33 (2021) 2105904, https://doi.org/10.1002/adma.202105904.

[59] M. Ismael, M. Wark, Perovskite-type LaFeO₃: photoelectrochemical properties and photocatalytic degradation of organic pollutants under visible light irradiation, Catalysts 9 (2019) 342, https://doi.org/10.3390/catal9040342.

[60] L. Hu, Y. Liao, D. Xia, F. Peng, L. Tan, S. Hu, C. Zheng, X. Lu, C. He, D. Shu, Engineered photocatalytic fuel cell with oxygen vacancies-rich rGO/BiO₁₋ₓI as photoanode and biomass-derived N-doped carbon as cathode: promotion of reactive oxygen species production via Fe²⁺/Fe³⁺ redox, Chem. Eng. J. 385 (2020) 123824, https://doi.org/10.1016/j.cej.2019.123824.

[61] Y. Zhu, Y. Zhuang, L. Wang, H. Tang, X. Meng, X. She, Constructing 0D/1D Ag₃PO₄/TiO₂ S-scheme heterojunction for efficient photodegradation and oxygen evolution, Chin. J. Catal. 43 (2022) 2558–2568, https://doi.org/10.1016/S1872-2067(22)64099-3.

[62] Y. Zhu, J. Ren, G. Huang, C. Dong, Y. Huang, P. Lu, H. Tang, Y. Liu, S. Shen, D. Yang, Red phosphorus grafted high-index (116) faceted anatase TiO₂ for Z-scheme photocatalytic pure water splitting, Adv. Funct. Mater. (2023) 2311623, https://doi.org/10.1002/adfm.202311623.